Angle-resolved x-ray photoemission from the valence bands of tungsten with high angular resolution and temperature variation

R. C. White, C. S. Fadley, and M. Sagurton*
Department of Chemistry, University of Hawaii at Manoa, Honolulu, Hawaii 98622

Z. Hussain
Department of Physics, University of Petroleum and Minerals, Dhahran 31261, Saudi Arabia
(Received 11 April 1986)

Angle-resolved valence photoemission spectra have been obtained for W(011) and W(001) using Al $K\alpha$ and Mg $K\alpha$ excitation and with both normal and off-normal emission directions. The angular resolution was $\lesssim \pm 1.0°$, and thus the highest to date in this energy regime, and the temperature also was varied from 295 to 1000 K. These spectra exhibit features very strongly dependent on emission direction and temperature that can be more precisely associated with direct-transition emission from different Brillouin-zone points than in prior studies. Data obtained at different temperatures are used to deconvolute direct- and nondirect-transition components. The direct-transition components are found to include residual intensity due to nondirect transitions. The simple direct-transition model applied previously to the analysis of such data is also extended to include the effects of correlated lattice vibrations via a cylindrical broadening in **k** space. This model is found to describe semiquantitatively the effects of phonon-assisted nondirect transitions on spectra.

INTRODUCTION AND THEORETICAL MODELS

Prior work of Hussain *et al.*[1,2] has shown that a simple direct-transition (DT) model incorporating free-electron final states and constant matrix elements is quite successful in describing the directional and photon-energy dependence of DT components in angle-resolved x-ray photoemission spectroscopy (ARXPS) spectra from the valence bands of tungsten. In addition, however, phonon-assisted nondirect transitions (NDT's) can play an important role in such valence spectra at higher photoelectron energies, as first pointed out by Shevchik.[3(a)] Shevchik's analysis was based on the theory of x-ray diffraction and the assumption of uncorrelated lattice vibrations, in which the atoms are taken to move independently of one another. This model results in a very simple form for the temperature dependence of the photocurrent $I(E,T)$, which can be written as the sum of temperature-*in*dependent DT and NDT components modulated by factors involving the Debye-Waller factor

$$W(T)=\exp[-g^2\overline{U^2}(T)/3] .$$

Here g is the magnitude of the reciprocal-lattice vector involved in the direct transition and $\overline{U^2}(T)$ is the three-dimensional mean-squared atomic displacement. The resultant expression for the photocurrent is[3(a)]

$$I(E,T)=W(T)I_{\rm DT}(E)+[1-W(T)]I_{\rm NDT}(E) . \quad (1)$$

Based on this model, Hussain *et al.*[1] have subsequently obtained ARXPS spectra from W(001) with Al $K\alpha$ excitation at several emission directions and temperatures and have found that Eq. (1) can be used in a self-consistent way with data for any two temperatures, T_1 and T_2, to extract empirical temperature-independent $I_{\rm DT}$ and $I_{\rm NDT}$ components for emission in a particular direction. The directional sensitivity of their spectra at lower temperatures was directly associated with DT emission from near various Brillouin-zone (BZ) points, but their experimental angular broadening of $\sim \pm 3.0°$ was too large to permit localizing the DT's to a very-well-defined region in the zone. This angular broadening effect on a typical set of XPS direct transitions is shown as the shaded discs in Fig. 1. Also shown here is the effect of the photon wave vector $\mathbf{k}_{h\nu}$ on the **k** conservation relation, the importance of which was verified in this prior study.[1] For the geometry of the present x-ray source and analyzer, $\mathbf{k}_{h\nu}$ for Al $K\alpha$ causes a shift of 1.61° between the measured $\mathbf{k}^f$ and $\mathbf{k}^i+\mathbf{g}$; for Mg $K\alpha$, this shift is 1.46°, as shown in Fig. 1.

In this paper, we go considerably beyond this earlier ARXPS work on W to study both Al $K\alpha$— and Mg $K\alpha$—excited emission from W(011) and W(001). An advantage of the (011) surface is that, unlike (001), it is not found to exhibit any surface reconstruction effects.[1,4] Also, we have used much higher angular resolutions than in prior XPS studies ($\lesssim \pm 1.5°$ compared to $\sim \pm 2.8°$–$3.5°$ previously), thus reducing the degree of zone averaging due to this effect by *at least* a factor of 4, and probably by more like a factor of 8, as discussed further below. Temperature dependence has again been studied as well, over the range from 295 (ambient) to 1000 K. The results have been interpreted in terms of the straightforward direct-transition model used previously by Hussain *et al.*,[1] but an attempt has also been made to more accurately allow for temperature-dependent phonon effects in this model. We briefly introduce this model before discussing our experimental procedure and results.

In proceeding further than the very simple picture of vibrational effects embodied in Eq. (1), we first note that,

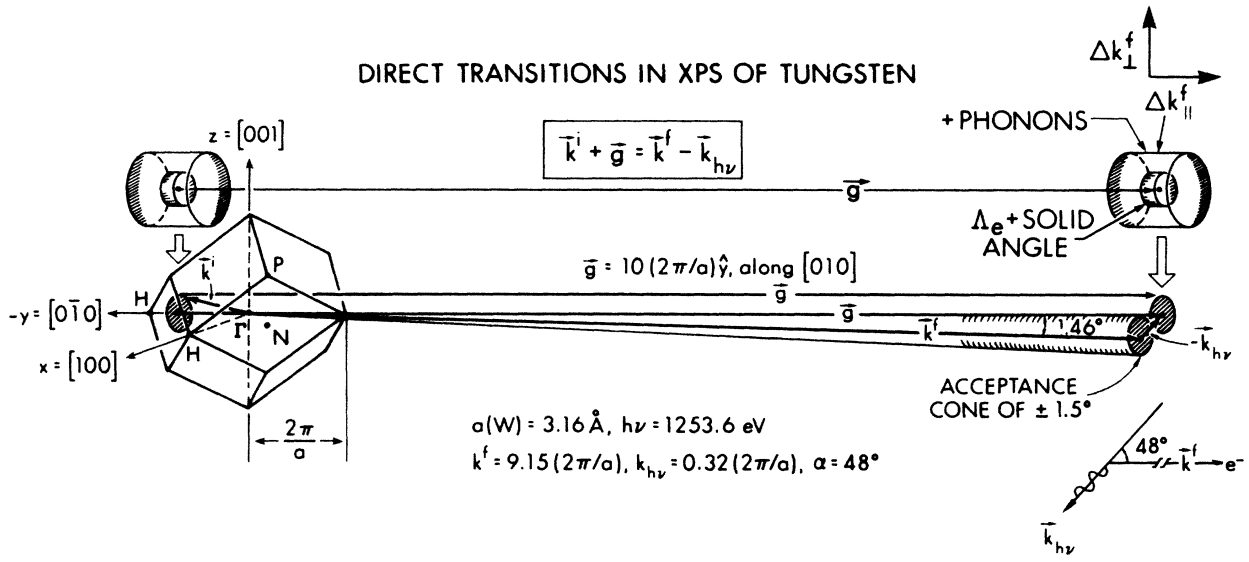

FIG. 1. The tungsten Brillouin zone (BZ), with a scale drawing of a **k**-conserving direct transition including photon wave vector $\mathbf{k}_{h\nu}$. Also indicated are the cylindrical broadenings in **k** space that are used to account for effects due to mean free path and angular resolution (inner cylinders), as well as phonon effects (outer cylinders). The experimental geometry as to photon incidence and electron exit is also shown.

by analogy with prior analyses of both x-ray diffraction[5] and electron diffraction,[6] the inclusion of correlated vibrations via phonons is expected to introduce nondirect transition intensity that is strongly peaked about the simple direct-transition point in the reduced zone. A similar conclusion has been reached by Shevchik[3(b)] via a theoretical analysis of angle-resolved photoemission based upon a tight-binding initial state, augmented plane wave (APW) final states, and sums over first-order phonon processes. This suggests immediately that the nondirect intensity need not be simply proportional to the total density of states (although this has been found to be very nearly true in prior ARXPS work[1]), and that Eq. (1) thus may be an oversimplification.

In a very recent theoretical study, Sagurton[7] has gone beyond the work of Shevchik by including correlated lattice vibrations and sums over all phonon modes in a calculation of photoemission current. A synopsis of this work is as follows: In general, the photocurrent for a given radiation polarization **A** can be written as[8]

$$I(\mathbf{k}^f, E=E^f) \propto v \sum_i \delta(E^f - E^i - h\nu) \, | \langle \mathbf{k}^f | \, \mathbf{A}\cdot\mathbf{p} \, | \mathbf{k}^i \rangle |^2 , \tag{2}$$

where E^f and E^i are the final and initial energies, respectively, $\mathbf{k}^f$ and $\mathbf{k}^i$ are the final and initial wave vectors (cf. Fig. 1), the δ function implies energy conservation, v is the photoelectron velocity in vacuum, and the standard dipole matrix element is $M_{if} \equiv \langle \mathbf{k}^f | \, \mathbf{A}\cdot\mathbf{p} \, | \mathbf{k}^i \rangle$. The model for calculating this current as a thermal average over all possible combinations of phonon excitations in M_{if} now further assumes that (1) the initial and final states are described within the muffin-tin approximation, (2) the excitation matrix element is dominated at XPS energies by the spatial regions within muffin-tin spheres, (3) the energies E^i and E^f and the forms of the wave functions ψ^i and ψ^f *within* the muffin tins are unchanged except in phase by the small vibrational displacements of the muffin-tin centers, and (4) the phonons can be described in a harmonic approximation. Assumption (3) is discussed by Shevchik[3(c)] and is equivalent in his notation to a dominance of "intra-atomic" electron-phonon effects. With several steps involving a final summation over all phonon modes of wave vector **q** and polarization $\hat{\epsilon}$, the matrix element M_{if} for an excitation from state i to state f in a displaced lattice characterized by a set of phonon amplitudes $A_{q\epsilon}$ becomes

$$M_{if} \propto m_{if} N \sum_{m=0}^{\infty} \left[\sum_{\substack{\{m^{\pm}_{q\hat{\epsilon}}\} \\ q\neq 0}} \delta(\mathbf{k}^f - \mathbf{k}^i - \mathbf{g} - \mathbf{k}_{h\nu} - \mathbf{Q}) \left[\prod_{q,\hat{\epsilon}} \frac{1}{m^{+}_{q\hat{\epsilon}}! m^{-}_{q\hat{\epsilon}}!} [-\tfrac{1}{2} A_{q\hat{\epsilon}} (\hat{\epsilon}\cdot\Delta\mathbf{k})]^{(m^{+}_{q\hat{\epsilon}} + m^{-}_{q\hat{\epsilon}})} e^{i(m^{+}_{q\hat{\epsilon}} - m^{-}_{q\hat{\epsilon}})\delta_{q\hat{\epsilon}}} \right] \right] , \tag{3}$$

where ω is the photon frequency, m_{if} is the dipole matrix element of Eq. (2) evaluated over a single muffin-tin sphere, N is the number of atoms in the solid, $\Delta\mathbf{k} = \mathbf{k}^f - \mathbf{k}^i$, $m^{+}_{q\hat{\epsilon}}$ ($m^{-}_{q\hat{\epsilon}}$) denotes the positive number of phonons of type $\mathbf{q},\hat{\epsilon}$ absorbed (emitted) in a given transition, m is the overall order of the phonon processes involved and is equal to $\sum_{q,\hat{\epsilon}} (m^{+}_{q\hat{\epsilon}} + m^{-}_{q\hat{\epsilon}})$, the inner summation is over all members of the set $\{m^{\pm}_{q\hat{\epsilon}}\}$ yielding the

same order m, $\mathbf{Q}$ is the net phonon momentum involved in a given excitation or $\sum_{\mathbf{q},\hat{\epsilon}}(m^{+}_{\mathbf{q}\hat{\epsilon}}-m^{-}_{\mathbf{q}\hat{\epsilon}})\mathbf{q}$, and $\delta_{\mathbf{q}\hat{\epsilon}}$ is the phase of phonon excitation $\mathbf{q},\hat{\epsilon}$. From Eq. (3), it can be shown[7] that the nondirect transitions due to phonon contributions for $\mathbf{q}\neq 0$ will be peaked about the direct transitions for $\mathbf{Q}=0$ due to the nature of the product over phonon amplitudes, each factor of which falls off rapidly for increasing $|\mathbf{q}|$. The expression for intensity in Eq. (2) [with Eq. (3) for the dipole matrix element] can then be averaged over phonon phases, thermally averaged, and summed over all occupied initial states i, leading to emission in a definite $\mathbf{k}^f$ to yield expressions for both the direct- and nondirect-transition currents. The resulting equation for direct-transition intensity is

$$I^{(0)}_{\mathrm{DT}}(E,T)\propto\frac{vN^2}{\omega^2}W(T)\sum_i\delta(E^f-E^i-h\nu)\times\delta(\mathbf{k}^f-\mathbf{k}^i-\mathbf{g}-\mathbf{k}_{h\nu})\,|\,m_{if}\,|^2\,, \tag{4}$$

which is essentially the same result as that obtained by Shevchik,[3] with all temperature dependence contained in the Debye-Waller factor. The nondirect-transition intensity is by contrast found to be more complex, as

$$I^{(0)}_{\mathrm{NDT}}(E,T)\propto\frac{vN^2}{\omega^2}\sum_i\delta(E^f-E^i-h\nu)W_i(T)\,|\,m_{if}\,|^2\sum_{\{m^{\pm}_{\mathbf{q}\hat{\epsilon}}\}}\delta(\mathbf{k}^f-\mathbf{k}^i-\mathbf{g}-\mathbf{k}_{h\nu}-\mathbf{Q})\langle\,|\,[\cdots]\,|^2\rangle\,, \tag{5}$$

where $\mathbf{Q}$ is now involved in wave-vector conservation, $W_i(T)$ is a Debye-Waller factor which may depend on the initial state through the varying $\mathbf{Q}$'s and thus $\mathbf{k}^i$'s that may lead to emission along $\mathbf{k}^f$, the set $\{m^{\pm}_{\mathbf{q}\hat{\epsilon}}\}$ is now restricted to those leading to the same $\mathbf{Q}$ for a given $\mathbf{k}^i$, and $\langle\,|\,[\cdots]\,|^2\rangle$ is the phase and thermal average of $|\,[\cdots]\,|^2$, where $[\cdots]$ is the product in square brackets on the right-hand side of Eq. (3). Here we use the superscript (0) to denote what are predicted to be pure direct-transition or pure nondirect-transition components of the total photoemission current. The inclusion of correlated lattice vibrations thus finally leads in this model to a different overall form of Eq. (1):

$$I(E,T)=W(T)I^{(0)}_{\mathrm{DT}}(E)+I^{(0)}_{\mathrm{NDT}}(E,T)\,. \tag{1'}$$

Here, the Debye-Waller factor has been factored out of $I^{(0)}_{\mathrm{DT}}(E,T)$, but no such simple factorization is possible in $I^{(0)}_{\mathrm{NDT}}(E,T)$.

In light of these results based upon a more accurate treatment of phonon-induced nondirect transitions in photoemission, the empirical deconvolution of experimental data into DT and NDT components according to Eq. (1) therefore implies that the components thus obtained be related to the pure DT and NDT components according to the more complex relations:

$$I_{\mathrm{DT}}(E)=I^{(0)}_{\mathrm{DT}}(E)+I^{(0)}_{\mathrm{NDT},1}(E,T)\,, \tag{6}$$

$$I_{\mathrm{NDT}}(E)=I^{(0)}_{\mathrm{NDT},2}(E,T)\,, \tag{7}$$

$$I^{(0)}_{\mathrm{NDT}}(E,T)=I^{(0)}_{\mathrm{NDT},1}(E,T)+I^{(0)}_{\mathrm{NDT},2}(E,T)\,. \tag{8}$$

Thus, the component I_{NDT} obtained via Eq. (1) may be only part of the total NDT contribution to the photoelectron spectrum, and the component I_{DT} obtained may contain a residual NDT contribution. The exact nature of the separation of $I^{(0)}_{\mathrm{NDT}}$ into $I^{(0)}_{\mathrm{NDT},1}$ and $I^{(0)}_{\mathrm{NDT},2}$ cannot be determined without a detailed evaluation of the phonon sums and resultant overall temperature dependences in Eq. (5). However, the existence of residual NDT intensity in I_{DT} components has been suggested in prior analyses of tungsten ARXPS data, where this intensity is furthermore found to resemble the total density of states (DOS).[1] In addition, very recent analyses of variable-temperature synchrotron radiation data for Pb(100) (Ref. 9), Pb(110) (Ref. 9), and Cu(001) (Ref. 10) in the energy interval $40\lesssim h\nu\lesssim 106$ eV indicates strong NDT contributions to such empirical I_{DT} components. Also, the presumed DT features in lower-energy angle-resolved ultraviolet photoemission spectroscopy (ARUPS) spectra from Cu and Ag are found to behave in a more complex way with temperature than the simple $W(T)$ of Eq. (1) would indicate.[11] We return to this below to consider the consequences of such analyses on the current results.

As an approximate method of including phonon-assisted nondirect transitions in the simple direct-transition model used previously by Hussain *et al.*[1] in analyzing ARXPS data, we consider below DT calculations in which a cylindrical broadening in $\mathbf{k}^i$ around a given DT point is included (cf. Fig. 1). This is intended to simulate the peaking of the nondirect transitions around the $\mathbf{k}_i$ value involved in the direct transition, with the expectation that higher-temperature data will require larger cylindrical broadenings for their description.

For reference in considering our data, Fig. 2(d) shows two different calculated band structures for tungsten. The solid bands are the result of a relativistic augmented plane wave (RAPW) calculation by Christensen and Feuerbacher (CF).[12] These are the values used as $E^i,\mathbf{k}^i$ inputs for our direct-transition calculations. The dashed bands are those of a more recent, fully self-consistent, relativistic calculation by Bylander and Kleinman (BK).[13] There are differences between the two which vary from 0.1 to 0.7 eV, and we discuss below certain shifts in the experimental direct-transition peaks that are of the same order of magnitude and in the correct directions to suggest that the BK calculation is more accurate. Based upon a prior study of Au,[14] these bands are expected to shift to lower E^i by $\lesssim 0.2$ eV due to lattice dilation effects over the 705-K range of our experiments. Figure 2(c) shows the CF total density of states as the solid curve. The dashed curve in this figure indicates the density of *occupied* levels as calculated with the CF band structure and then broadened by a Gaussian to simulate the instrumental resolution of ~ 0.9 eV.

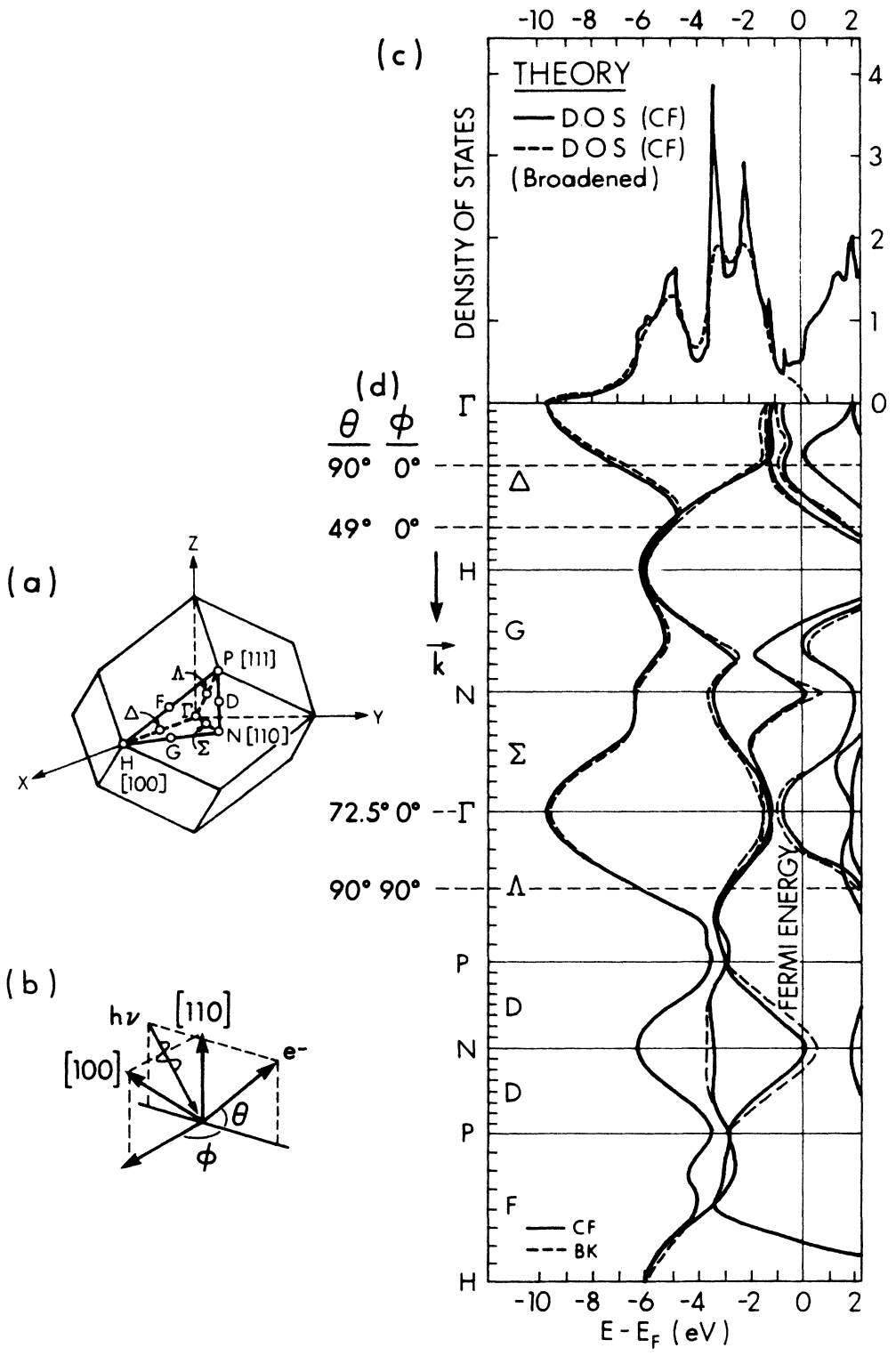

FIG. 2. (a) The tungsten Brillouin zone, with various high-symmetry points and directions labeled. (b) The experimental geometry for measurements on a (011) surface, with the angles θ and ϕ defined. In experiments on a (001) surface, θ is again measured with respect to the surface, and ϕ with respect to a [100] azimuth in the surface. (c) The theoretical density of states for tungsten. The solid curve is an unbroadened curve due to Christensen and Feuerbacher in Ref. 12 (CF). The dashed curve is the same density of *occupied* states, broadened by a Gaussian of 0.9 eV FWHM to simulate experimental resolution. (d) Theoretical tungsten band structures. The solid bands are those of CF, while the dashed bands are the more recent calculation by Bylander and Kleinman in Ref. 13 (BK). The dashed lines across the bands are placed at BZ points around which various experimental spectra originate, with the corresponding θ,ϕ combinations with Al $K\alpha$ excitation from W(011) also indicated.

EXPERIMENTAL PROCEDURE

The ARXPS measurements were performed on a VG ESCALAB5 spectrometer equipped with a custom-built two-axis specimen goniometer of $\sim\pm0.3°$ accuracy.[15,16] Nonmonochromatized radiation was used for excitation, with a resolution for the Ag $3d_{5/2}$ reference peak of 0.91 eV for both Al $K\alpha$ at 1486.6 eV and Mg $K\alpha$ at 1253.6 eV.

This spectrometer was additionally modified with an externally-selectable tube-array collimator to provide for a very-well-defined angular acceptance in which *all* trajectories are within $\pm1.5°$ of the mean emission direction. This collimator consists of an array of stainless-steel tubes with length-to-diameter ratio chosen to limit trajectories to within a $\pm1.5°$ cone. For the resulting rigorous exclusion of all trajectories outside of $\pm1.5°$, a detailed calculation of the geometric properties of such an array[16] shows that the angular divergence as averaged over emission from all specimen surface points is only $\pm0.6°$. Retardation of the photoelectrons to 10—20 eV before analysis also may result in some loss of intensity due to enhanced deflection angles. Thus, our effective angular acceptance is certainly $\lesssim\pm1.5°$, and probably more like $\pm1.0°$. Comparing with prior experiments at a much more approximately defined ±2.8—$3.5°$ thus indicates a considerable reduction of $\lesssim1/(2.8)^2\approx1/8$ in the amount of zone averaging. From the example Mg $K\alpha$ transitions in Fig. 1, a deflection of 1.0° corresponds to a shift of $\sim0.16(2\pi/a)$ in the position of $\mathbf{k}^f$ and thus also $\mathbf{k}^i$ [that is, a distance of $\sim\frac{1}{6}$ the Brillouin-zone (BZ) radius].

Both the (011) and (001) tungsten crystals were oriented to within $\pm0.3°$ of their respective directions, and cleaned using procedures discussed elsewhere.[1] Base pressures during experiments were maintained between 2×10^{-11} and 5×10^{-11} torr at ambient temperature, and at $\lesssim1\times10^{-10}$ torr for sample temperatures of up to 1000 K. Crystal surfaces were cleaned before experiments by high temperature ($\sim$2000 °C) flash heating, after which surface contaminants were below levels detectable by XPS. The accumulation of contaminants such as C or O during any experiment reported here totaled $<3\%$ of a monolayer. The definitions of the polar (θ) and azimuthal (ϕ) angles of emission above the (011) surface are shown in Fig. 2(b); for the (001) surface, θ is again measured with respect to the surface and ϕ with respect to a [100] direction lying in the surface, exactly as in prior work by Hussain *et al.*[1] Due to the very high sensitivity of ARXPS valence-band spectra to small changes in emission direction[1] (especially in view of the high angular resolutions to be used here), a very accurate and reproducible alignment of the crystal axes with respect to the tube array axis (which is the same as the entry lens axis) was critical. This alignment was performed with an accuracy of $\lesssim\pm0.3°$ by first calibrating the θ with ϕ scales with W $4f$ core-level x-ray photoelec- tron diffraction (XPD) patterns as a function of polar and azimuthal angles; these high-resolution XPD curves exhibit very fine features of only a few degrees in width that can be used for such calibrations.[1,14,15]

As an illustration of the dramatic effect of increased angular resolution of such ARXPS spectra, Fig. 3 compares ambient-temperature Mg $K\alpha$—excited spectra from W(001) at $\theta=76.0°$, $\phi=0.0°$ obtained with the $\pm1.5°$ tube array in place and with only the standard lens-entry aperture which approximately limits angles to $\pm6.0°$. The two spectra are markedly different, with the high-resolution curve having its strongest peak at ~5.1 eV, whereas the low-resolution curve has its maximum at ~2.4 eV. The low-resolution curve also resembles the density of states [cf. Fig. 2(c)], suggesting nearly complete averaging over the Brillouin zone. The high-resolution spectrum also is striking in comparison to previous ARXPS results from W in showing a much greater relative enhancement of the peak at ~5.1 eV; in prior data with a resolution of $\sim\pm2.8°$, where the analogous feature is seen at ~4.8 eV, it is never found to be the most intense peak.[1] All subsequent spectra reported here will be with the $\pm1.5°$ tube array.

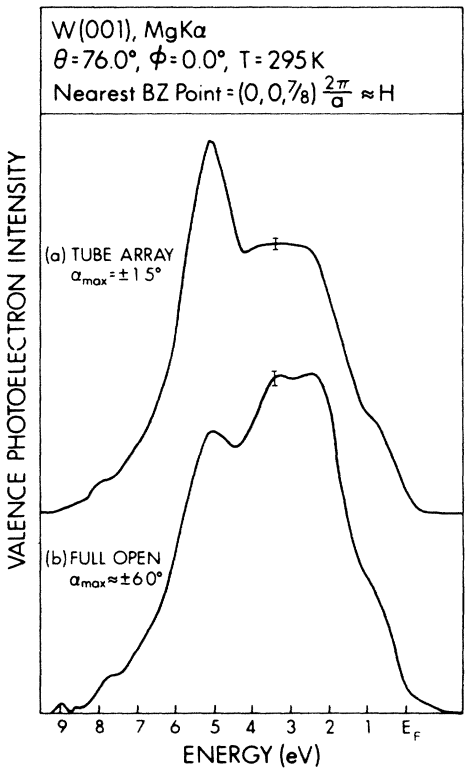

FIG. 3. The effect of increased angular resolution on Mg $K\alpha$—excited spectra from W(001) at ambient temperature. In (a) a tube-array collimator with upper limits of $\pm1.5°$ is used, and in (b) the single aperture of $\sim\pm6.0°$ that is standard for the instrument is the only angle-defining device. In (a) simple direct transitions originate from around the H point. In (b) rather complete zone averaging is evident.

RESULTS AND DISCUSSION

A. W(011) with Al $K\alpha$ excitation

Figures 4 and 5 show high-angular-resolution ARXPS data obtained at both 295 K [Figs. 4(b) and 5(b)] and 1000 K [Figs. 4(a) and 5(a)], along with the relevant Debye-Waller factors of 0.55 and 0.14, respectively. Emission is

along two different emission direction 23.5° apart that have been chosen via calculations based upon the simple DT model used previously[1] to yield $\mathbf{k}^i$ values that are centered as nearly as possible on the H and Γ points in the BZ. The central BZ point sampled according to the DT model is given in units of $1/8(2\pi/a)$ on these and subsequent figures. Figures 4 and 5 illustrate that there is a much greater sensitivity of the ambient-temperature spectra to emission direction than is seen in the prior work on W by Hussain *et al.*,[1] with the H-point and Γ-point spectra here having markedly different shapes. This enhanced sensitivity is due to the lower degree of zone averaging associated with higher angular resolution. Smaller differences between spectra are also still seen at 1000 K, especially in the region of the strong H-point peak at 5.3 eV. This result also is not surprising in view of the $\sim 14\%$ of direct transitions still expected on the basis of the simple Shevchik model.

These temperature-dependent spectra have also been used as in Ref. 1 to extract I_{DT} and I_{NDT} components via Eq. (1). These DT and NDT components are shown in curves (*c*) and (*d*), respectively, of Figs. 4 and 5. The DT components are sharpened considerably compared to the corresponding ambient-temperature spectra, whereas the NDT components are very close to the high-temperature spectra. This result is expected, since W is only 0.14 at the high temperature, and $1-W$ therefore is 0.86 and reasonably close to unity. The NDT components also closely resemble the DOS, as noted before by Hussain *et al.*[1]

We now consider the simplest DT-model simulation of DT components such as those in Figs. 4(c) and 5(c). If we neglect the effects of phonons, this simulation involves $\mathbf{k}$ broadening due to only two sources: finite angular resolution and inelastic scattering. For example, in Fig. 1, we show as shaded discs the amount of broadening in $\mathbf{k}$ space required to allow for an angular acceptance cone of 1.5° half angle; note also that this broadening is in directions perpendicular to $\mathbf{k}^f$, and will be specified by a value $\pm\Delta k_{\perp}^f$. For a full $\pm 1.5°$ acceptance, this results in a disc diameter of $0.53(2\pi/a)$ for Al $K\alpha$ and $0.48(2\pi/a)$ for Mg $K\alpha$. A plus-minus translation of this disc in a direction parallel to $\mathbf{k}_f$ must also be included to account for additional broadening due to the photoelectron inelastic mean free path, which is taken to be 15.5 Å for Al $K\alpha$ excitation and 14.2 Å for Mg $K\alpha$ excitation. The amount of $\mathbf{k}^f$ broadening due to Λ_e is calculated on the basis of exponential decay from $2\Delta k_{||}^f = 2\pi(0.55)/\Lambda_e$.[17] This leads to the flat, inner cylinders shown in Fig. 1, which have thicknesses along $\mathbf{k}^f$ of $2\Delta k_{||}^f \approx 0.12(2\pi/a)$. It is thus evident that inelastic broadening is a much smaller effect than angular acceptance broadening at such XPS energies, although the converse is true in UPS measurements at ~ 40–100 eV.[10] For comparison to experiment in Figs. 4 and 5, direct-transition calculations have been performed with an angular broadening of $\pm 1.1°$ that is more

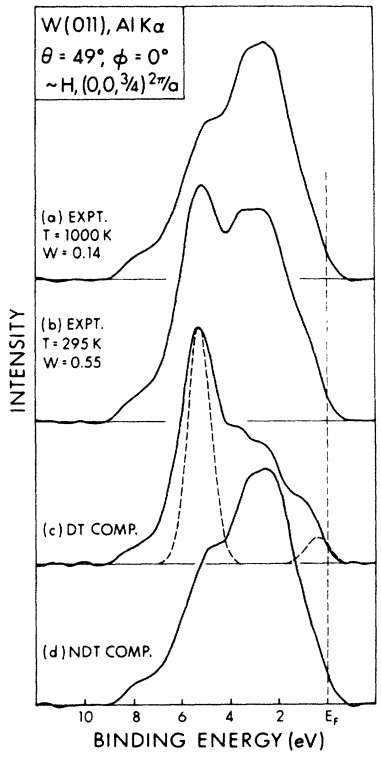

FIG. 4. Temperature-dependent Al $K\alpha$–excited experimental spectra from W(011) at (a) 1000 K and (b) 295 K, along with (c) direct-transition (DT) and (d) nondirect-transition (NDT) components derived via Eq. (1). Here simple DT's originate from near the H point. A calculated direct transition curve including only angular resolution and mean-free-path broadening in $\mathbf{k}$ is shown dashed with the empirical DT component in (c).

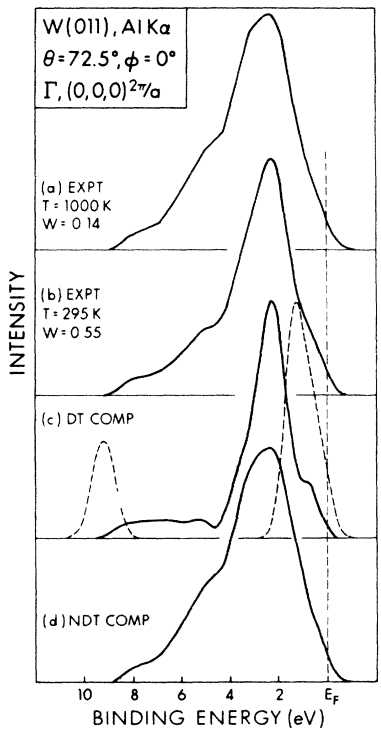

FIG. 5. Same as Fig. 4, but for DT emission centered near the Γ point.

representative of the smaller effective experimental broadening. These calculations are based on strict conservation of energy and wave vector, and include summations over a uniform three-dimensional distribution of 500—30 000 $\mathbf{k}^i$ points within flat, inner cylinders such as those in Fig. 1. [Phonon contributions to energy conservation are assumed to be negligible, as is implied in Eq. (5)]. An overall Gaussian energy broadening of 0.9 eV full width at half maximum (FWHM) was included at the end of each calculation to simulate instrumental resolution, as with the DOS in Fig. 2(c).

The results of such calculations are compared directly to empirical DT components in Figs. 4(c) and 5(c). It is readily seen from these comparisons that, when reasonable estimates are made for these two minimum contributions to $\mathbf{k}$-space broadening, the strongest peaks in the DT components obtained from the deconvolution procedure agree rather well with the dominant peaks in the DT calculations as to shape, and, to a lesser degree, also as to position. The H-point agreement is excellent as to the feature at 5.3 eV, whereas the main Γ-point feature is predicted to be ~ 1.1 eV too low in binding energy. Some of this discrepancy (~ 0.4 eV) can be ascribed to the difference between the CF and the more accurate BK band structures near the Γ point [cf. Fig. 2(d)]. However, in addition, the DT components in Figs. 4(c) and 5(c) appear to include some NDT-like intensity at least qualitatively resembling the DOS, and we will shortly consider methods for allowing this.

Similar deconvolutions of empirical DT and NDT components have been performed for all of the data points presented here, as well as for spectra originating near three other BZ points not along high symmetry directions, two for Al $K\alpha$ excitation from W(011) and one for Mg $K\alpha$ excitation from W(001). In all cases, the results were similar to those presented in Figs. 4 and 5. That is, the ambient-temperature spectra are dominated by peaks expected from simple DT theory, while the high-temperature spectra have an overall DOS-like appearance, but still exhibit small differences from one another. Empirical DT components in all cases also show some residual NDT contribution, as suggested by Eq. (6), with an appearance similar to Fig. 4(c) whenever the dominant DT peak occurs at a binding energy $\gtrsim 4$ eV, or similar to Fig. 5(c) when the dominant DT peak is well above 4 eV. Empirical NDT components all resemble the high-temperature spectra, and the DOS, as seen before in Figs. 4(a) and 4(d) and Figs. 5(a) and 5(d). In fact, the empirical NDT components shown in these figures represent the extremes in variation of all those thus obtained. All NDT components show dominant intensity over ~ 2.0—3.5 eV and a strong shoulder over ~ 4.5—5.5 eV, with much weaker shoulders from ~ 0.0—0.8 eV and ~ 7.0—9.0 eV that are both expected to be of s-p origin. The major difference among the empirical NDT components is the ratio of the intensity at 2.0—3.5 eV to that at 4.5—5.5 eV. This ratio varies from a minimum of ~ 1.5 [Fig. 4(d)] to a maximum of ~ 2.0 [Fig. 5(d)] depending upon the relative strength for the DT intensity at 4.5—5.5 eV. Thus, it is clear that empirical NDT components isolated in this way do reflect to some degree the zone point around which DT emission occurs.

There are two straightforward options for proceeding from here within the direct-transition model so as to arrive at a simple, but reasonably correct, inclusion of both DT and NDT contributions. First, we can attempt to adjust the experimental DT component obtained via Eq. (1) by subtracting from it some percentage of the experimental NDT component obtained via the same analysis, until empirically optimum agreement is obtained between the calculated DT component with minimum broadening and the adjusted experimental DT component. This approach results in an adjusted experimental DT component given by

$$I_{\mathrm{DT(adj)}}(E)=I_{\mathrm{DT}}(E)-CI_{\mathrm{NDT}}(E)\ , \tag{9}$$

where C is an adjustable constant, and it thus makes the assumption that $I^{(0)}_{\mathrm{NDT},1}(E,T)$ and $I^{(0)}_{\mathrm{NDT},2}(E,T)$ in Eqs. (6) and (7) are somehow of the same functional form. Although $I_{\mathrm{NDT}}(E)=I^{(0)}_{\mathrm{NDT},2}(E,T)$ and resembles the DOS, we have seen that this changes somewhat with emission direction [cf. Figs. 4(d) and 5(d)]. As a second procedure, we can extend the averaging in $\mathbf{k}$ space of the DT calculation in an attempt to directly model phonon effects as qualitatively expected from a more accurate model including correlated lattice vibrations. As introduced briefly before, this extension of the DT model has been accomplished by using a three-dimensional, cylindrical, isotropic broadening in $\mathbf{k}$ space centered about the inner cylinder already assumed to describe minimal broadening due to angular resolution and the mean free path. Such broadening is shown by the outer cylinders in Fig. 1. This model thus correctly concentrates the nondirect transitions around the direct transition in $\mathbf{k}$ space. We have performed such DT calculations for successively larger cylinders, extending the broadening in equal steps of $\pm 0.05(2\pi/a)$ in both the directions perpendicular to and parallel to $\mathbf{k}^f$, with all increments being in addition to the minimum inner cylinder dimensions. Empirically, we can then choose the best match between such calculations and the experimental DT component from Eq. (1) without any adjustment according to Eq. (9). Both of these methods are applied to interpreting the data presented below.

In Figs. 6—8, we show spectra representing emission which the simple DT model predicts to be centered at BZ points along the Γ-Δ-H line, and in Fig. 9, spectra centered at one point along Λ [cf. Fig. 2(a)]. The precise emission directions (that is, the θ and ϕ values) and the exact locations of the central emission points in $\mathbf{k}^i$ are indicated on each figure. Each of these four figures shows the same four types of curves: for (a), the empirical DT component from Eq. (1); for (b), the result of a DT calculation with an optimized degree of additional cylindrical broadening to account for residual NDT effects; for (c), a DT component adjusted according to Eq. (9), with the C value indicated; and for (d), the result of a DT calculation with minimum cylindrical broadening due to an angular acceptance of $\pm 1.1°$ and the electron mean free path [the same as the dashed curves in Figs. 4(c) and 5(c)]. The central BZ point for each one of these four figures is also indicated as a horizontal dashed line on the band structures of Fig. 2(d).

Consider first the H-point emission in Fig. 6. Figure 6(b) shows an isotropically-broadened DT calculation corresponding to an averaging over $\sim 27\%$ of the BZ. For comparison, the DT calculation including only angular and mean-free-path broadening [Fig. 6(d)] corresponds to a volume of only 0.3% of the BZ, in principle a very desirable condition for band mapping if there was no phonon contribution. There is quite good agreement between Figs. 6(a) and 6(b), particularly if allowance is made for the difference of 0.12 eV between the CF and more accurate BK band positions, as indicated by the vertical fiducial marks. Also shown in Fig. 6(c) is the adjusted experimental DT component, $I_{\mathrm{DT,(adj)}}$, obtained via Eq. (9) with an optimum $C=0.50$ so that 50% of the NDT component obtained via Eq. (1) [shown in Fig. 4(d)] is subtracted from the DT component shown in Fig. 6(a). The agreement is again very good between Figs. 6(c) and 6(d), with the slight shift of the mean peak again being explainable in terms of the BK band structure. However, some residual intensity between ~ 1.8 and 4.5 eV in the adjusted experimental DT component is not accounted for by the minimally-broadened DT calculation.

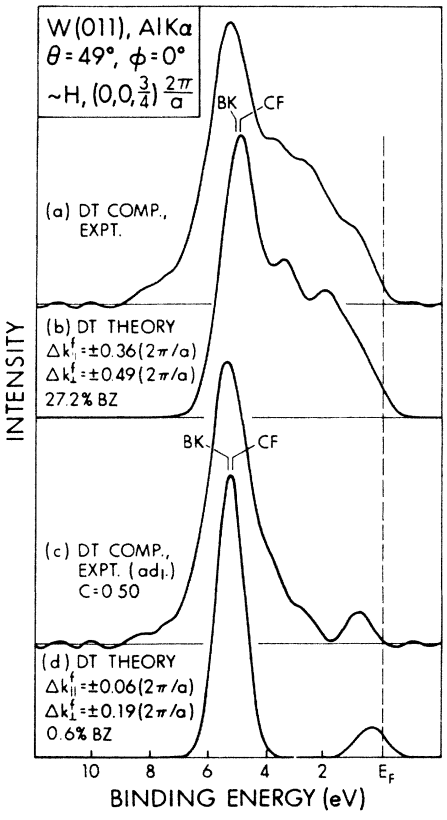

FIG. 6. (a) Empirical direct-transition component obtained via Eq. (1) for emission centered near the H point [same as Fig. 4(c)]. (b) DT calculation including cylindrical broadening to simulate photon-assisted nondirect transitions, as described in text. (c) Adjusted empirical DT component via Eq. (9). (d) Simple DT calculation allowing for only angular resolution and mean-free-path broadening in $\mathbf{k}$.

To provide some idea as to how uniquely the degree of cylindrical averaging in Fig. 6(b) could be chosen, we show in Fig. 10 a series of theoretical curves for the emission geometry of Fig. 6 with varying degrees of such averaging. These curves begin at the bottom of the figure with the minimally-broadened case of Fig. 6(d) and generally represent increasing the size of the cylinder by $0.10(2\pi/a)$ in both the $\pm\Delta k_{\perp}^{f}$ and $\pm\Delta k_{\parallel}^{f}$ directions up to a limit where a DOS-like curve is reached. The DOS is also shown for comparison at the top of the figure. These results make it very clear that the empirical degree of averaging can be chosen to within $\sim 27\pm 10\%$. Note also that the major peak at ~ 5.0 eV shows only a relatively subtle shift of ~ 0.3 eV to lower binding energy as broadening increases, although all other features change dramatically.

Figure 7 shows the same four curves as Fig. 6, but this time for emission normal to the (011) surface that is predicted to originate from near a Δ-type BZ point $\sim\frac{3}{8}$ of the distance from Γ to H. The agreement between Fig. 7(a) and the cylindrically-broadened DT calculation in Fig. 7(b) is quite good, especially if cross-section effects that would act to diminish the relative intensity due to the more s,p mixed bands below ~ 4 eV are taken into account. A shift in the main peak at ~ 2.3 eV is again explained by the difference between the BK and CF band structures. A weaker feature at ~ 5.2 eV is present in Figs. 7(a) and 7(b); only the shoulder observed at ~ 0.5 eV

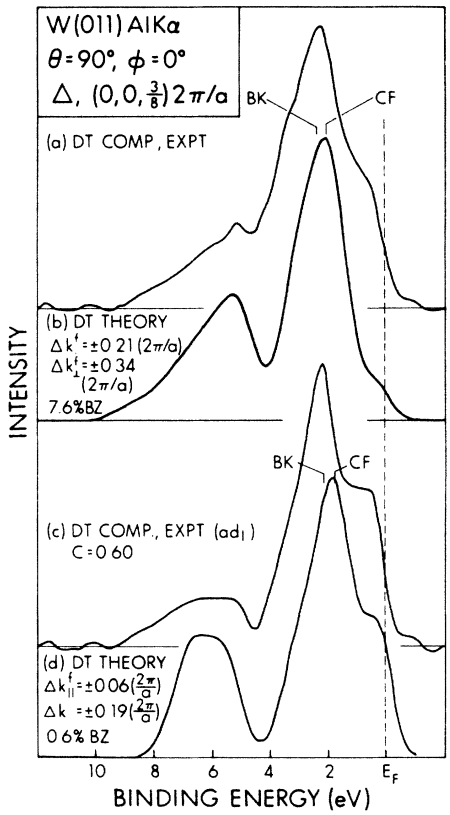

FIG. 7. Same as Fig. 6, but for DT emission centered on a Δ point.

is not seen as strongly in Fig. 7(b). The broadening in Fig. 7(b) to allow for residual NDT effects corresponds to ~8% of the BZ, and is thus somewhat less than that required for optimum agreement for emission from the *H* point. Comparison of the adjusted DT curve in Fig. 7(c) with minimally-broadened DT theory in Fig. 7(d) also yields excellent agreement, again provided that cross-section effects and the evidently more accurate BK band structure are taken into account. Here, the shoulder at ~0.4–0.5 eV is also correctly predicted by theory. For this Δ point, the best agreement is obtained by subtracting 60% of the NDT component from the DT component of Fig. 6(a), a value rather close to that used at the *H* point.

Figure 8 shows the same treatment for the data given in Fig. 5. Note that, in comparing Figs. 8(a) and 8(b), a broadening of the calculation over ~18% of the BZ is sufficient to again obtain good agreement with the experimental DT component, with a peak shift that can again be ascribed to the less-accurate CF band structure again being seen. The adjusted experimental DT component of Fig. 8(c) was obtained here by subtracting only 10% of the experimental NDT component ($C=0.10$) from Fig. 8(a), an amount which is significantly less than that needed for the *H* or Δ points. Also, this adjusted curve does not agree well with the minimally-broadened DT calculation, even if the predicted peak shift between band structures is considered. The dominant peaks in Figs. 8(c) and 8(d) are different in position by ~1.0 eV, and the peak positions of the weaker *s,p*-band features at higher binding energies are off by ~2.0 eV. This suggests that some form of residual three-dimensional broadening in **k** space due to phonons is present even in the adjusted data, and also that manipulation of the data according to Eq. (9) is not a fully reliable approach, since it does not work equally well for all BZ points. The cylindrical broadening of the DT calculation used in Fig. 8(b) by contrast seems to semiquantitatively describe the effects of phonons in such empirical DT spectra.

Figure 11 provides a further indication of the origin of the peak shifts seen between the curves in Figs. 8(c) and 8(d). Here, a set of theoretical curves analogous to those in Fig. 10 is shown for the emission geometry of Fig. 8. The empirical degree of cylindrical averaging can here be determined to be within ~19±10%, with both the *s,p* features at high binding energy *and* the dominant peak at ~1–2 eV exhibiting large shifts with increased broadening. Between minimal broadening [as in Fig. 8(d)] and 27%, the dominant peak shifts by ~0.9 eV; this shift is thus sufficient to explain the good agreement between Figs. 8(a) and 8(b), and the poor agreement between Figs. 8(c) and 8(d). The relatively small shift of the main peak with broadening in Fig. 10 by contrast explains why both pairs of curves there agrees rather well. The shift and broadening of the *s,p*-band peak at higher binding energy is also correctly predicted in Fig. 11. Thus, it is clear that

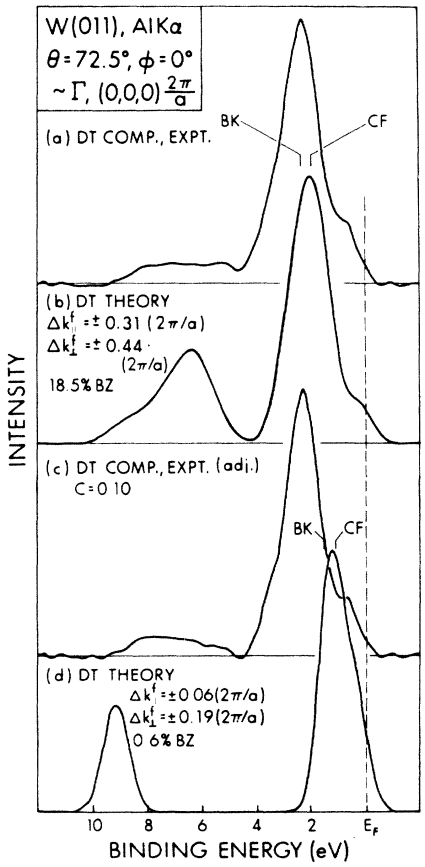

FIG. 8. Same as Fig. 6, but for DT emission centered on the Γ point.

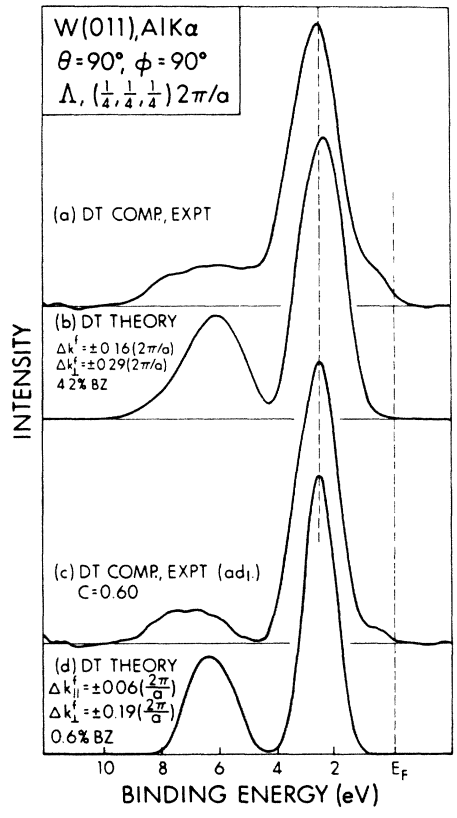

FIG. 9. Same as Fig. 6, but for DT emission centered on a Λ point.

different zone points may exhibit differing degrees of peak shifts due to the presence of nondirect transitions, and that such effects can make comparisons to simple DT theory with minimal broadening somewhat unreliable.

Lastly, in Fig. 9, we show another set of Al $K\alpha$–excited data taken for normal emission, but with a rotation in ϕ of 90° from that of Fig. 7. Only the effect of the photon wave vector (cf. Fig. 1) makes this data not symmetry equivalent to that of Fig. 7, and ultimately leads to emission from near Λ. Here the agreement is quite good for both methods of comparing experiment and DT theory. The close agreement between the CF and BK bands in this region [cf. Fig. 2(d)] is also consistent with the very small peak shifts seen here. Figure 9(b) also represents the least cylindrical broadening needed for any of the data presented, corresponding to only ~4% of the BZ. Figure 9(c) was obtained by subtracting 40% of the NDT component from the DT component of Fig. 9(a), a number more in line with the amount needed for the Δ and H points.

The four sets of data for Al $K\alpha$-excited emission discussed up to this point are also of interest in that they correspond to direct transitions associated with quite different **g** values. The **g**'s and their magnitudes are as follows:

$$H(\text{Fig. 6})-\mathbf{g}=(11,0,1)(2\pi/a)\ ,\quad |\mathbf{g}|=10.30(2\pi/a)\ ,$$

$$\Delta(\text{Fig. 7})-(7,0,7)(2\pi/a),\quad 9.90(2\pi/a)\ ;$$

$$\Gamma(\text{Fig. 8})-(9,0,5)(2\pi/a),\quad 11.04(2\pi/a)\ ,$$

and

$$\Lambda(\text{Fig. 9})-(7,0,7)(2\pi/a),\quad 9.90(2\pi/a)$$

(as for Δ by symmetry). This range of **g** values yields ambient-temperature bulk Debye-Waller factors of 0.47–0.54. The 0.55 value quoted here is based on an estimated $|\mathbf{g}|=(2mE^f/\hbar^2)^{1/2}$.

As a final comment on this method of allowing for nondirect transitions via cylindrical **k** broadening, we consider the alternative of directly describing ambient-temperature spectra with broadened DT calculations without trying to isolate DT and NDT components. A comparison of such broadened DT calculations (e.g., those in Figs. 10 and 11) to ambient-temperature spectra for all six BZ points observed from W(011) [e.g., Figs. 4(b) and 5(b)] shows reasonable agreement for averaging over ~40% to ~75% of the BZ for all cases. Here, the match

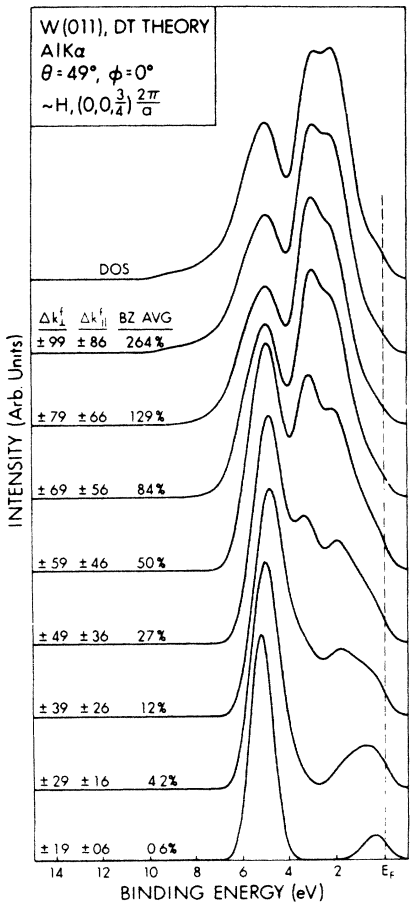

FIG. 10. Effect of increased cylindrical broadening in **k** space to allow for phonon-assisted nondirect transitions on DT calculations for emission centered near the H point. The geometry is identical to that of Fig. 6. The density of states is also shown for comparison. The units of $\Delta k_\perp^f$ and $\Delta k_\parallel^f$ are again $2\pi/a$.

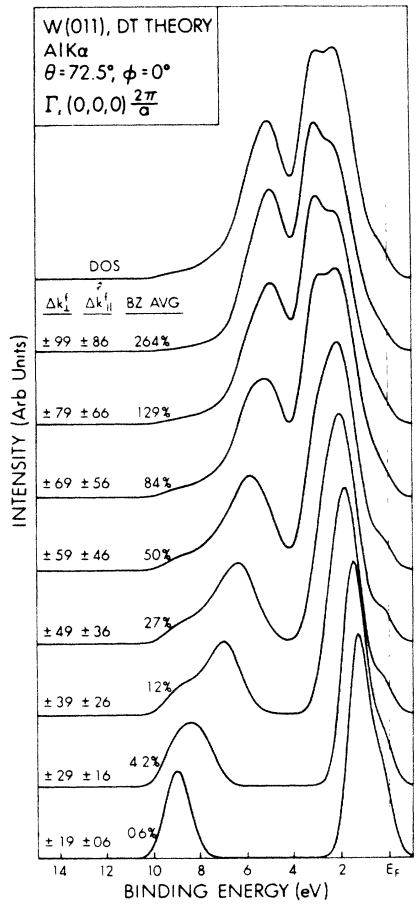

FIG. 11. As Fig. 10, but for emission centered at the Γ point.

between theory and experiment is not as good as that obtained between such broadened DT calculations and empirical DT components. Compare, for example, Fig. 4(b) with Fig. 10 and Fig. 5(b) with Fig. 11. However, in general, the overall widths and positions of principal features in ambient spectra are well reproduced by the broadened calculations, although the relative intensities of peaks are not always correct. This result is not surprising in view of our neglect of matrix-element effects. Such a comparison of experiment to broadened DT theory essentially asks that the temperature dependence of both $I_{\mathrm{NDT},1}$ and $I_{\mathrm{NDT},2}$ [cf. Eq. (8)] be described totally by a simple isotropic broadening in **k** space which does not include any matrix-element effects. Hussain *et al.*[1] were reasonably successful in describing lower-angular-resolution spectra at ambient temperature by a weighted sum of DT calculations and the total DOS, but also did not consistently obtain the correct relative intensities from the calculation.

By contrast, the degree of success obtained here in comparing isotropically-broadened DT calculations with empirical DT components suggests that $I^{(0)}_{\mathrm{NDT},1}(E,T)$ [Eqs. (6) and (8)] can be reasonably well described by this approach, even though matrix-element effects could certainly still be important in quantitatively predicting peak relative intensities. The higher angular resolution in the present study has also permitted better determination of both the DT and NDT components than was previously possible.

As a final important aspect of our experimental data, we have measured the change in integrated valence-band intensity (that is, the total photocurrent in the region of $\sim$0—12 eV after background subtraction) on going from ambient temperature to 1000 K. The low- and high-temperature data were obtained in back-to-back runs with no change in specimen alignment or surface conditions. Specifically, these results show that the ratio of high-temperature—to—low-temperature intensity ($I_{\mathrm{HT}}/I_{\mathrm{LT}}$) for DT emission from near H (cf. Fig. 6) is 0.96, for Δ(cf. Fig. 7) is 1.01, for Γ (cf. Fig. 8) is 1.02, and for emission from another nearby Λ point [$\sim(0.0,\frac{1}{2})2\pi/a$] accessed with a much different emission direction ($\theta=66°$, $\phi=0°$) is 0.95. The clustering of these results to within experimental error around unity (0.99 ± 0.04), even though the spectral shapes change markedly in some cases [cf. Figs. 4(a) and 4(b)], thus shows that for tungsten in this energy regime, direct-transition intensity must be lost at very nearly the same rate as nondirect-transition intensity is gained with increasing temperature. This empirical "sum rule" is consistent with the form of the simple Shevchik model as expressed in Eq. (1). Also, an expansion of $I^{(0)}_{\mathrm{NDT}}$ in Eq. (5) including only first-order phonon effects ($m=1$) is found to predict the same 1:1 relationship between DT loss and NDT gain,[7] and more specifically that the ratio of NDT intensity to DT intensity will be given by $(1-W)/W$, just as suggested by Eq. (1) via a much more approximate analysis. More experimental data concerning this point would certainly be of interest, for example, involving a broader temperature range where higher-order processes could become important and/or other initial BZ points.

B. W(001) with Mg $K\alpha$ excitation

As concluding comparisons of experiment and DT theory, we show in Figs. 12 and 13 results obtained with Mg $K\alpha$ excitation from a W(001) crystal. Again, calculations based on simple DT theory have been used to select emission geometries for which well-defined BZ points are sampled. In Fig. 12, emission from very near H is involved, and in Fig. 13 from very near Γ. Temperature-dependent data have again been used with Eq. (1) to derive DT components, which are shown in Figs. 12(a) and 13(a). DT theory with adjustable cylindrical broadening to allow for residual NDT effects has then been used to optimally describe the DT components, as shown in Figs. 12(b) and 13(b). The agreement between panels (a) and (b) in both cases is very good, with the major peak positions very well predicted and the general form of the weaker features also in good agreement [e.g., the shoulder at 0.3—0.5 eV in Figs. 13(a) and 13(b)]. The degree of zone averaging required is 25% in both cases. The results in Figs. 12 and 13 are also extremely self-consistent with their H and Γ counterparts from W(011) with Al $K\alpha$ excitation in Figs. 6 and 8, respectively. The empirical DT components are very close between Figs. 6(a) and 12(b) and Figs. 8(a) and 13(a), as also are the theoretical curves in Figs. 6(b) and 12(b) and Figs. 8(b) and 13(b). The degrees of zone averaging in the latter are also very similar, at 27% and 25%, and 19% and 25%, respectively. These comparisons thus make it clear that, even for an arbitrary choice of surface, photon energy, and emission geometry with respect to the crystal axes, the simple DT model permits uniquely locating experimental transitions very close to high-symmetry BZ points such as H and Γ. Also, the simple cylindrical zone-averaging scheme appears to provide a rather good and self-consistent description of empirical DT components originating at such zone points, even though such averaging is found to affect peak posi-

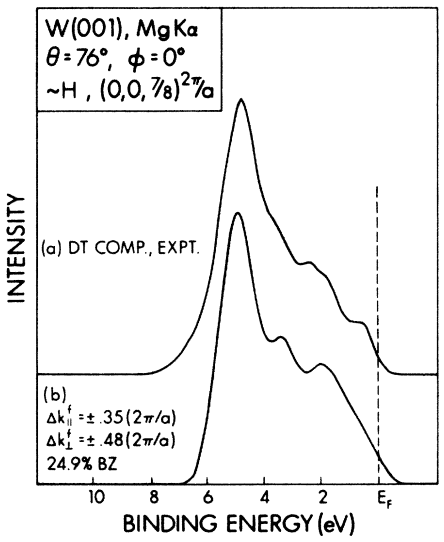

FIG. 12. As Figs. 6(a) and 6(b), but for Mg $K\alpha$ excitation from W(001) in a direction such that DT emission is centered near the H point.

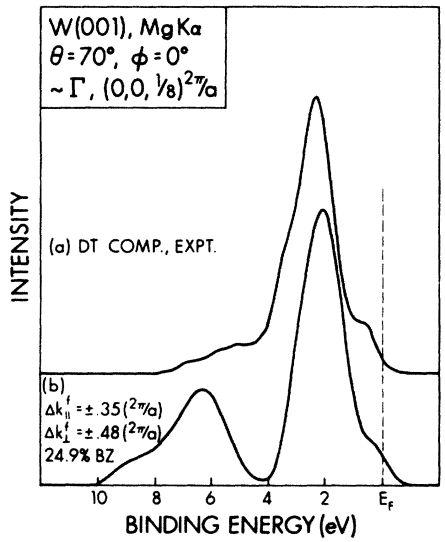

FIG. 13. As Figs. 8(a) and 8(b), but for Mg $K\alpha$ excitation from W(001) in a direction such that DT emission is centered near the Γ point.

tions and widths to a much different degree for the two cases explored here (cf. Figs. 10 and 11).

As for W(011), emission from a BZ point not located along a high-symmetry direction also has been considered for Mg $K\alpha$-induced emission from W(001). Temperature-dependent emission from near $(0,\frac{3}{8},\frac{1}{2})2\pi/a$ occurring for $\theta=52°$, $\phi=0°$ has been separated into DT and NDT components, and cylindrically-broadened DT calculations are found to compare quite favorably with the empirical DT component broadening over ~ 15–20% of the BZ. This degree of broadening is thus consistent with the other data presented here, and with the overall observation that the broadening volumes needed are $\sim 15\% \pm 9\%$, with smaller values being appropriate for points that are well away from high-symmetry points in the reduced zone.

CONCLUSIONS

In conclusion, we have found that using much higher angular resolutions of $\sim \pm 1.0°$ in ARXPS measurements on tungsten yields much greater sensitivity to both emission direction and temperature than seen in prior studies. High-temperature spectra obtained at 1000 K resemble the density of states, in agreement with earlier data, but are still found to retain some direct-transition character. Temperature-dependent data can be used to approximately decompose spectra into direct-transition (DT) and nondirect-transition (NDT) components. Also, a simple direct-transition model with constant matrix elements and a free-electron final-state dispersion relation is found to predict very well the Brillouin-zone point around which the allowed direct transitions are centered for a variety of emission directions, for emission from both W(011) and W(001), and for excitation with both Al $K\alpha$ and Mg $K\alpha$ radiation.

However, it is clear that the temperature dependence of the NDT components is not as simple as assumed in earlier analyses, and that this leads to the inclusion of NDT intensity in the DT components. A more accurate treatment of phonon-assisted nondirect transitions also suggests that residual NDT-like intensity will remain in such empirical DT components. As a simple model of such NDT effects, a cylindrical broadening in $\mathbf{k}$ space about the simple direct transition is used. This is found to predict rather well most of the features in the empirical DT components, and to explain certain peak shifts observed between experiment and theory. It is also possible to conclude on the basis of these comparisons that the band structure of Bylander and Kleinman is more accurate than the earlier work of Feuerbacher and Christensen. The empirical amounts of BZ averaging remaining in such DT components are found to be between 4% and 27% of the zone, but no precise physical meaning can be given to these numbers without a more accurate model for phonon-assisted nondirect transitions. Measurements of *total* valence spectrum intensities also suggest constancy with temperature, or equivalently that intensity lost from direct transitions must appear as nondirect transitions.

This work thus represents the most precise study of E versus $\mathbf{k}$ values to date using ARXPS, which has in most prior studies been confined to density-of-states-like measurements. Although tungsten is a somewhat special case in being expected to yield a majority of direct transitions at ambient temperature (cf. Table I in Ref. 1), it is clearly of interest in future studies to look at this and other materials with higher-energy resolution, high angular resolution, and at cryogenic temperatures. This should permit much more precise $E,\mathbf{k}$ determinations to be made, as well as a more quantitative assessment of the roles of nondirect transitions and angular acceptance broadening as limiting factors in determining how well band structures can be studied in this energy regime. It is also clear that more quantitative theoretical calculations of nondirect-transition effects via sums over various phonon-assisted processes are very important for understanding such temperature-dependent valence spectra.

ACKNOWLEDGMENT

This work was supported by National Science Foundation Grant No. CHE-83-20200.

*Present address: National Synchrotron Light Source, Brookhaven National Laboratory, Upton, NY 11973-5000.

[1]Z. Hussain, S. Kono, L.-G. Petersson, C. S. Fadley, and L. F. Wagner, Phys. Rev. B **23**, 724 (1981).

[2]Z. Hussain, E. Umbach, J. J. Barton, J. G. Tobin, and D. A. Shirley, Phys. Rev. B **25**, 672 (1982).

[3](a) N. J. Shevchik, J. Phys. C **10**, L555 (1977); (b) Phys. Rev. B **16**, 3428 (1977); (c) **20**, 3020 (1979).

[4](a) T. E. Felter, R. A. Barker, and P. J. Estrup, Phys. Rev. Lett. **38**, 1138 (1977); (b) C. R. Brundle, in *The Chemical*

Physics of Solid Surfaces and Heterogeneous Catalysis, edited by D. A. King and D. P. Woodruff (Elsevier, New York, in press), Vol. 3.

[5](a) B. E. Warren, *X-ray Diffraction* (Addison-Wesley, Reading, Mass., 1969), pp. 159—169; (b) R. W. James, *The Optical Principles of the Diffraction of X-rays* (Glasgow University Press, Glasgow, Scotland, 1954), pp. 193—228.

[6]J. T. McKinney, E. R. Jones, and M. B. Webb, Phys. Rev. **160**, 523 (1967).

[7]M. Sagurton (unpublished results). See also, a more detailed discussion of this theoretical treatment of phonon effects by R. C. White, C. S. Fadley, M. Sagurton, P. Roubin, D. Chandesri, J. Lecante, C. Guillot, and Z. Hussain, Phys. Rev. B (to be published).

[8]P. J. Feibelman and D. E. Eastman, Phys. Rev. B **10**, 4932 (1974).

[9]G. Jezequel, A. Barski, P. Steiner, F. Solal, P. Roubin, R. Pinchaux, and Y. Petroff, Phys. Rev. B **30**, 4833 (1984).

[10]R. C. White, C. S. Fadley, M. Sagurton, P. Roubin, D. Chandesri, J. Lecante, C. Guillot, and Z. Hussain, Solid State Commun. **50**, 633 (1986); Phys. Rev. B (to be published).

[11]H. Mårtensson and P. O. Nilsson, Surf. Sci. **152**, 189 (1985), and references therein.

[12]N. Christensen and B. Feuerbacher, Phys. Rev. B **10**, 2349 (1974).

[13]D. M. Bylander and L. Kleinman, Phys. Rev. B **29**, 1534 (1984).

[14]N. E. Christensen, Phys. Rev. B **20**, 3205 (1979).

[15]C. S. Fadley, Prog. Surf. Sci. **16**, 275 (1984).

[16]R. C. White, R. Trehan, and C. S. Fadley, J. Electron Spectrosc. (to be published).

[17]J. J. Barton and D. A. Shirley (unpublished).